23

Comparison between Different Supply Port Configurations in Gas Journal Bearings

Federico Colombo, Terenziano Raparelli and Vladimir Viktorov
Politecnico di Torino, Department of Mechanics
Italy

1. Introduction

Because of their precision, gas bearings are widely used for very high speed spindle applications. Compared to conventional oil bearings, gas bearings generate less heat and do not pollute the environment. Air viscosity is three orders of magnitude lower than oil, so the power dissipated in gas bearings is very low. The major disadvantage of these bearings is rotor whirl instability, which restricts the possible range of applications.
Researchers have studied this problem using different methods since the '60s. Gross first applied a perturbation method to evaluate the stability of an infinitely long journal bearing (Gross & Zachmanaglou, 1961). Galerkin's method was used by others to calculate rotor speed and mass at the stability threshold (Cheng & Pan, 1965). Lund investigated the stiffness and damping coefficients of hydrostatic gas bearing, and used these coefficients to investigate whirl instability (Lund, 1968). Wadhwa et al. adapted the perturbation method to calculate the dynamic coefficients and to study the stability of a rotor supported by orifice compensated gas bearings (Wadhwa et al., 1983). Results show that aerostatic bearings have a larger load capacity and higher stability than plain journal bearings. Han et al. proved that more circumferential supply ports result in increased stiffness coefficient but reduced damping (Han et al., 1994). Others found that orifice-compensated and shallow-pocket type hybrid gas journal bearings offer better stability than eight-orifice type bearings (Zhang & Chang, 1995).
Also porous journal bearings were studied (Sun, 1975) and compared against hybrid gas bearings with multi-array entries (Su & Lie, 2006), (Heller et al., 1971). Despite the fact that damping is generally higher in porous bearings than in aerostatic bearings, the results of (Su & Lie, 2006) suggest that at high operating speeds, multi-array entry bearings are more stable than porous bearings.
Other studies (Andres, 1990), (Sawcki et al., 1997), (Yoshikawa et al., 1999) considered various pressurized air compensated configurations, but very few papers analysed the influence of the number and location of entry ports.
In (Su & Lie, 2003) hybrid air journal bearings with multi-array supply orifices were compared to porous bearings. One to five rows of orifices were considered. It was found that five rows of supply orifices perform as well as porous bearings, whilst supply orifice feeding has the advantage of consuming less power than porous feeding. Paper (Yang et al., 2009) compared bearing systems with double-array orifice restrictions to three and six entry

systems. Results show that the stability threshold is better with six-ports than with three ports.
In (Colombo et al., 2009) the authors analysed two externally pressurized gas bearings, one with a central row of supply orifices, the other with a double row. The supply port downstream pressure was found to be proportional to the critical mass. At this pressure reading, the second bearing type was 30% stiffer and 50% more stable.
The aim of this work is to compare three externally pressurized gas journal bearings at given air consumption rates. The idea was to investigate which offers the best spatial distribution of supply orifices under the same pneumatic power. The study compared radial stiffness and pressure distribution for the three bearing types, also evaluating the damping factor and the whirl ratio of the shaft. The stability threshold was calculated for different restriction parameters so that the proposed bearing types could be compared.

2. Description of the problem

The object of the study was a rigid rotor supported by two identical gas journal bearings situated symmetrically with respect to the journal centre. The rotor, with diameter D=50 mm, was considered to be perfectly balanced. The radial air clearance was h_0=20 μm and the bearings had L/D ratio equal to unity.
Three bearing types were considered, as illustrated in figure 1. Bearing type 1 featured four supply ports situated in the centre plane of the bearing; bearing type 2 featured two sets of supply ports, situated at $z=L/4$ and $z=3L/4$; bearing type 3 also featured a central vented circumferential chamber.
The three bearing types were comparable in terms of stiffness and damping coefficients, air consumption and stability. In (Colombo et al., 2009) the authors compared bearing types 1 and 2 (see figure 1) considering the same supply port diameter d_s. The bearing with double array entries (bearing type 2) was found to be 30% stiffer than the one with a single central array (bearing type 1) but the air consumption was two times as much. Moreover, bearing 2 was more stable: the rotor mass at incipient whirl instability was about 50% greater.
Another point of interest was which bearing type was to be preferred for the same level of air consumption. In this paper the bearings illustrated in figure 1 were compared considering different supply port diameters in order to have the same air consumption.

3. Lubrication analysis

3.1 Mathematical model

The two-degree-of-freedom rotor equations of motion are shown in (1). The rotor mass is m. As the shaft was assumed to have cylindrical motion, gyroscopic effects and tilting inertia moments are non-existent. The second member of the equations is zero because the rotor was assumed to be perfectly balanced and there were no external forces applied to it. This was the most unstable condition, as shown in (Belforte et al., 1999).

$$\begin{cases} m\ddot{x} + 2\int_0^L \int_0^{2\pi} p(z,\theta)\cos\theta r d\theta dz = 0 \\ m\ddot{y} + 2\int_0^L \int_0^{2\pi} p(z,\theta)\sin\theta r d\theta dz = 0 \end{cases} \tag{1}$$

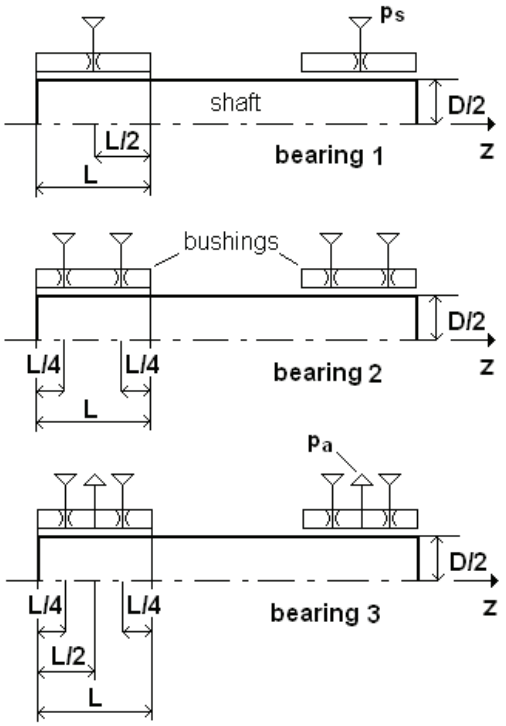

Fig. 1. Bearing types under study

The pressure distribution in clearance h was calculated solving the distributed parameters problem described by the Reynolds equation for a compressible-fluid-film journal bearing (2), assuming isothermal gas expansion.

$$\frac{\partial}{\partial z}\left(ph^3\frac{\partial p}{\partial z}\right)+\frac{\partial}{r\partial\theta}\left(ph^3\frac{\partial p}{r\partial\theta}\right)+12\mu R^0T^0\frac{G}{rdrd\theta}=6\mu\omega\frac{\partial(ph)}{\partial\theta}+12\mu\frac{\partial(ph)}{\partial t} \tag{2}$$

Mass flow rate G at supply orifice was calculated in accordance with the isentropic expansion formula (3), corrected by experimentally identified discharge coefficient c_d, expressed by eq. (4). Reynolds number at the supply hole was calculated as per equation (5). Formula (4) is the result of an extensive set of experimental tests carried out on air pads with different inherence parameters (Belforte et al., 2008).

$$G=c_d\pi\frac{d_s^2}{4}p_s\sqrt{\frac{k}{k-1}\left[\left(\frac{p_c}{p_s}\right)^{\frac{2}{k}}-\left(\frac{p_c}{p_s}\right)^{\frac{k+1}{k}}\right]\frac{2}{RT}}\quad if\ \frac{p_c}{p_s}\geq b$$

$$G=c_d\pi\frac{d_s^2}{4}p_s\sqrt{\frac{k}{k+1}\left(\frac{2}{k+1}\right)^{\frac{2}{k-1}}\frac{2}{R^0T^0}}\quad \text{if}\ \frac{p_c}{p_s}<b \tag{3}$$

$$c_d = 0.85\left(1 - e^{-8.2\frac{h}{d_s}}\right)\left(1 - e^{-0.001Re}\right) \tag{4}$$

$$Re = \frac{4G}{\pi d_s \mu} \tag{5}$$

Assuming a cylindrical shaft motion, the clearance may be expressed by the following:

$$h(z) = h_0\left(1 - \varepsilon_x \cos\theta - \varepsilon_y \sin\theta\right) \tag{6}$$

3.2 Solution method

The Reynolds equation was discretized using a finite difference method along directions z and θ for integration over the fluid film. A rectangular grid with equi-spaced nodes in both directions was considered. The number of nodes in the axial (index i) and circumferential (index j) directions were n and m respectively. Equation (2) may be written for each node as follows:

$$\begin{aligned} &p_{i+1,j}^2\left(a_{i,j} + b_{i,j}\right) + p_{i-1,j}^2\left(a_{i,j} - b_{i,j}\right) + p_{i,j+1}^2\left(c_{i,j} + d_{i,j}\right) + p_{i,j-1}^2\left(c_{i,j} - d_{i,j}\right) + \\ &-2p_{i,j}^2\left(a_{i,j} + c_{i,j}\right) + \left(p_{i,j+1} - p_{i,j-1}\right)e_{i,j} - p_{i,j}\left(g_{i,j} + 24\mu\frac{h_{i,j}^t - h_{i,j}^{t-1}}{\Delta t}\right) + \\ &+G_{i,j}\frac{24\mu R^0 T^0}{r\Delta\theta\Delta z} = 24\mu h_{i,j}^t \frac{p_{i,j}^{t+1} - p_{i,j}^t}{\Delta t} \end{aligned} \tag{7}$$

where,

$$a_{i,j} = \frac{h_{i,j}^3}{\Delta z^2} \qquad b_{i,j} = \frac{3h_{i,j}^2}{2\Delta z}\left(\frac{\partial h}{\partial z}\right)_{i,j}$$

$$c_{i,j} = \frac{h_{i,j}^3}{r^2\Delta\theta^2} \qquad d_{i,j} = \frac{3h_{i,j}^2}{2r^2\Delta\theta}\left(\frac{\partial h}{\partial \theta}\right)_{i,j}$$

$$e_{i,j} = 6\mu\omega\frac{h_{i,j}}{\Delta\theta} \qquad g_{i,j} = 12\mu\omega\left(\frac{\partial h}{\partial \theta}\right)_{i,j}$$

At the supply port $G_{i,j}$ was calculated using equation (3), whereas elsewhere it was zero. The boundary conditions imposed were:

- $p=p_a$ at $z=0$ and $z=L$; for bearing type 3 $p=p_a$ also at $z=L/2$
- periodic condition at $\theta=0$ and $\theta=2\pi$.

The Euler explicit method was used, so equation (7) becomes:

$$p_{i,j}^{t+1} = p_{i,j}^t + \Delta t \cdot f\left[p_{i,j}^t, p_{i,j+1}^t, p_{i,j-1}^t, p_{i+1,j}^t, p_{i-1,j}^t, h_{i,j}^t, h_{i,j}^{t-1}, \left(\frac{\partial h}{\partial \theta}\right)_{i,j}^t, \left(\frac{\partial h}{\partial z}\right)_{i,j}^t\right] \tag{8}$$

The system of nxm equations (8) was solved together with equations (3) to (6) and rotor equations of motion (1).

The solution procedure started with a set of input data (shaft diameter, radial clearance, bearing axial length, position and diameter of supply orifices, shaft speed).
To calculate the static pressure distribution, h was maintained constant in time and the system was solved with initial condition $p_{i,j}=p_a$ for each node.
Pressure distribution was evaluated at each time step and the bearing forces acting on the shaft were updated in equation (1). Thus, the rotor trajectory was determined starting with the initial static pressure distribution and using the following set of initial conditions:

$$x(0)=h_0\varepsilon_x(0);\ y(0)=h_0\varepsilon_y(0)$$

$$\dot{x}(0)=h_0\dot{\varepsilon}_x(0);\ \dot{y}(0)=h_0\dot{\varepsilon}_y(0)$$

3.3 Mesh size and time step definition

Calculations were made with different mesh sizes and the results were compared for optimum trade-off between computational time and accuracy of the solution.
The grids are detailed in table 1.

nxm	*Δz (mm)*	*rΔθ (mm)*
13x24	4.17	6.54
17x32	3.12	4.91
25x48	2.08	3.27
49x96	1.04	1.64

Table 1. Mesh sizes used in calculations; r=25 mm, L/D=1

Figure 2 shows the axial and circumferential pressure distributions obtained for bearing type 1 with different numbers of grid points. If the number of grid points is increased, the pressure distribution becomes more clearly defined, but the difference is almost negligible. Only at the supply ports, where pressure gradients are high, the difference is more marked. The grid selected for calculation was n=49, m=96.

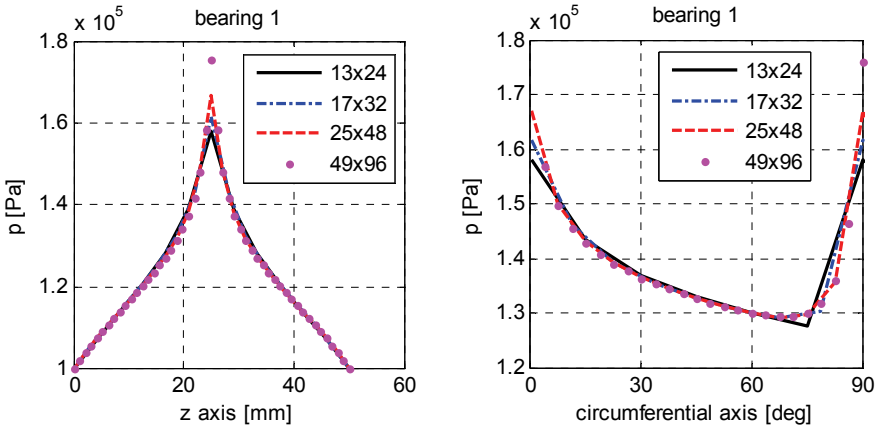

Fig. 2. Axial and circumferential pressure distributions for bearing type 1 obtained with different mesh grids; h_0=20 μm, p_s=5·10^5 Pa rel., d_s=0.1 mm, ω=60 krpm, ε=0

Euler explicit method was used to solve the time progression of the system. The rotor trajectories obtained with different time steps Δt are compared in figure 3.
The rotor initial conditions were:

$$\varepsilon_x(0)=0;\varepsilon_y(0)=0$$

$$\dot{\varepsilon}_x(0)=0;\dot{\varepsilon}_y(0)=0$$

The trajectories are increasingly adjacent with decreasing Δt. The time step used in the paper was Δt=10^{-7} s.

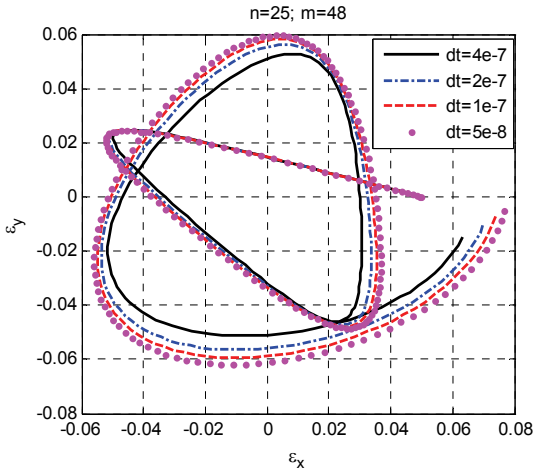

Fig. 3. Rotor trajectories with bearing type 1 obtained with different time steps and grid 25x48; initial conditions specified by $\varepsilon_x(0)$=0.05, $\varepsilon_y(0)$=0, $\dot{\varepsilon}_x(0)=0, \dot{\varepsilon}_y(0)=0$, h_0=20 μm, p_s=5·10^5 Pa rel., d_s=0.1 mm, ω=60 krpm

4. Discussion and results

4.1 Resistance analysis

The air supply system may be described with an equivalent lumped parameters system, illustrated in figure 4.
Orifice restriction resistance R_s is related to the supply ports and decreases with increasing diameter d_s. It may be calculated using linearizing expression (3) with respect to downstream pressure p_c. Clearance resistance R_h depends on clearance h_0, on bearing dimensions size and on the arrangement of the supply ports. It is obtained by solving the distributed parameters problem and calculating pressure distribution in the clearance.
Imposing mass continuity in the lumped parameters system of figure 4, supply port downstream pressure p_c can be obtained by

$$p_c = p_s - \frac{R_s}{R_s + R_h}(p_s - p_a) \tag{9}$$

This pressure depends both on the supply system and on clearance: at reduced d_s, supply port downstream pressure p_c approximates ambient pressure p_a, whereas with increased d_s it approaches supply pressure p_s.
Analysis of resistances at different supply pressures with the shaft rotating in central position was performed for bearings 1 and 2 in (Colombo et al., 2009) which shows the relationship between supply port diameter d_s and downstream pressure p_c, confirming that the influence of bearing number Λ on p_c with rotor in centred position is almost negligible, and air consumption is almost independent of speed.

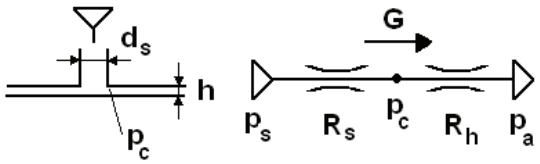

Fig. 4. Lumped parameters model of the restriction and clearance resistances

4.2 Air consumption

The three bearings of figure 1 were compared in terms of air consumption, as shown in figure 5. The air mass flow was calculated as a function of the clearance for different supply port diameters. At reduced d_s, the air consumption for bearing types 2 and 3 was quite identical. Only for d_s=0.2 mm a difference was noted at reduced clearance. The air flow in different bearings (for different resistance R_h) was found to be the same for supply orifices in critical conditions, when air flow is only a function of p_s.
As air consumption is a function of d_s and h_0, the supply ports diameter is determined at specific rates of air consumption G, as shown in table 2.
Bearing type 1 was not considered for the last two values of G because the volume of air passing through its orifices when p_c=p_s (in this condition R_s=0) was lower than these values.

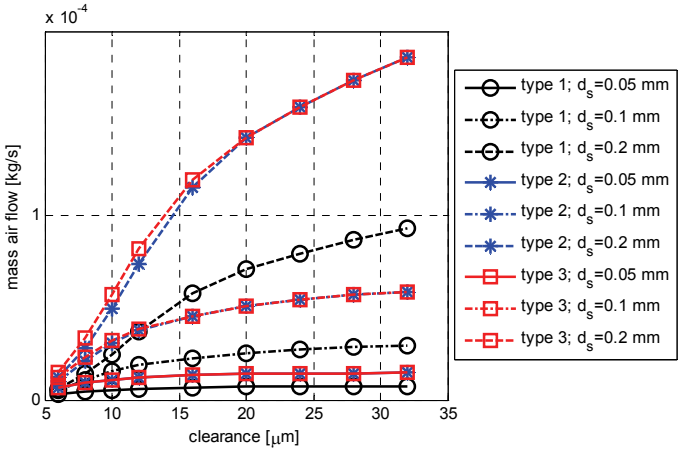

Fig. 5. Air consumption of the three bearings vs. air clearance for different supply port diameters; calculations are for Λ=0 and with rotor in central position; p_s=5·10^5 Pa rel.

bearing type	diameter d_s [mm]	air flow $G \cdot 10^4$ [kg/s]
1	0.155	0.5
2	0.1	
3	0.1	
1	0.383	1.42
2	0.2	
3	0.2	
1	0.8	2.14
2	0.282	
3	0.275	
2	0.4	2.94
3	0.372	
2	0.6	4.28
3	0.8	

Table 2. Supply port diameter d_s considered in calculations for the three bearings at different air consumption G; $p_s=5 \cdot 10^5$ Pa rel.

4.3 Pressure distribution

Figures 6 and 7 compare the axial and circumferential pressure distributions in the three bearings with rotor in central position and restriction parameters specified in table 2. Bearing type 1 shows a lower ratio R_s/R_h than the other bearings because its maximum pressure is the highest. At $G=0.5 \cdot 10^{-4}$ kg/s all bearings have orifices in sonic conditions, being $p_c/p_s<b$. At $G=2.14 \cdot 10^{-4}$ kg/s bearing type 1 is near saturation condition ($p_c \simeq p_s$). Speed stretches the circumferential pressure profile toward the direction of rotation, as visible in figure 7.

4.4 Bearing stiffness

Bearing stiffness was calculated by imposing a shaft displacement of 1 μm along direction x and evaluating the bearing reaction force.
Bearing stiffness k was

$$k = \sqrt{k_{xx}^2 + k_{xy}^2} \tag{10}$$

where the stiffness coefficients calculated in steady-state conditions were

$$k_{xx} = \frac{F_x}{h_0 \varepsilon_x} = \frac{\int_0^L \int_0^{2\pi} p(z,\theta) \cos\theta r d\theta dz}{h_0 \varepsilon_x}$$

$$k_{xy} = \frac{F_y}{h_0 \varepsilon_x} = \frac{\int_0^L \int_0^{2\pi} p(z,\theta) \sin\theta r d\theta dz}{h_0 \varepsilon_x}$$

Non-dimensional stiffness k^*, given by

$$k^* = k \frac{h_0}{p_a L D} \tag{11}$$

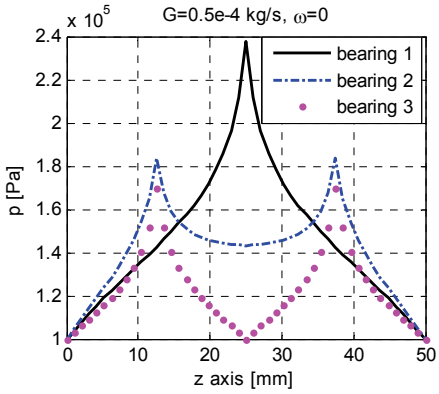
x 10^5
G=0.5e-4 kg/s, ω=0
bearing 1
bearing 2
bearing 3
p [Pa]
z axis [mm]

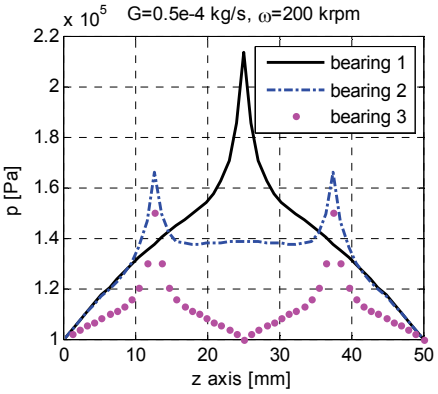
x 10^5
G=0.5e-4 kg/s, ω=200 krpm
bearing 1
bearing 2
bearing 3
p [Pa]
z axis [mm]

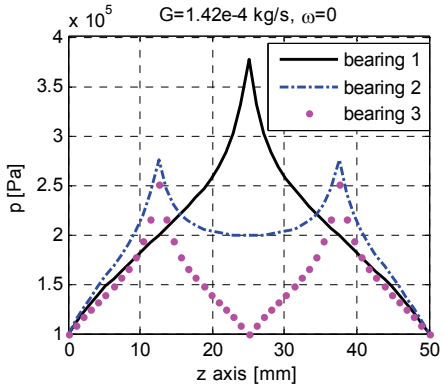
x 10^5
G=1.42e-4 kg/s, ω=0
bearing 1
bearing 2
bearing 3
p [Pa]
z axis [mm]

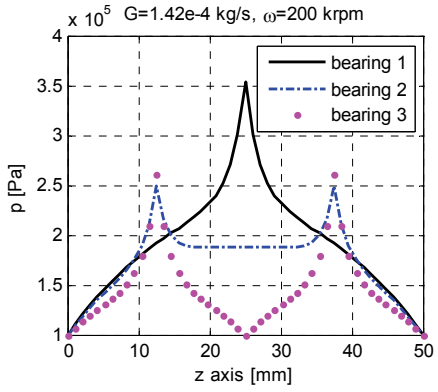
x 10^5
G=1.42e-4 kg/s, ω=200 krpm
bearing 1
bearing 2
bearing 3
p [Pa]
z axis [mm]

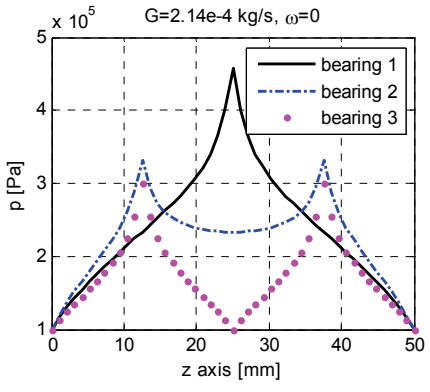
x 10^5
G=2.14e-4 kg/s, ω=0
bearing 1
bearing 2
bearing 3
p [Pa]
z axis [mm]

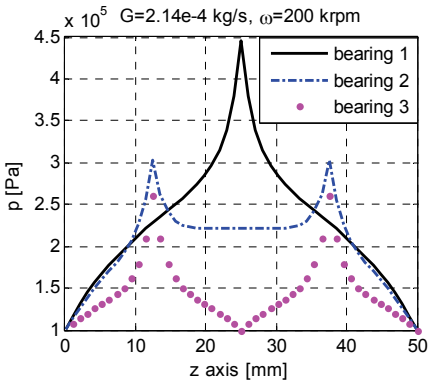
x 10^5
G=2.14e-4 kg/s, ω=200 krpm
bearing 1
bearing 2
bearing 3
p [Pa]
z axis [mm]

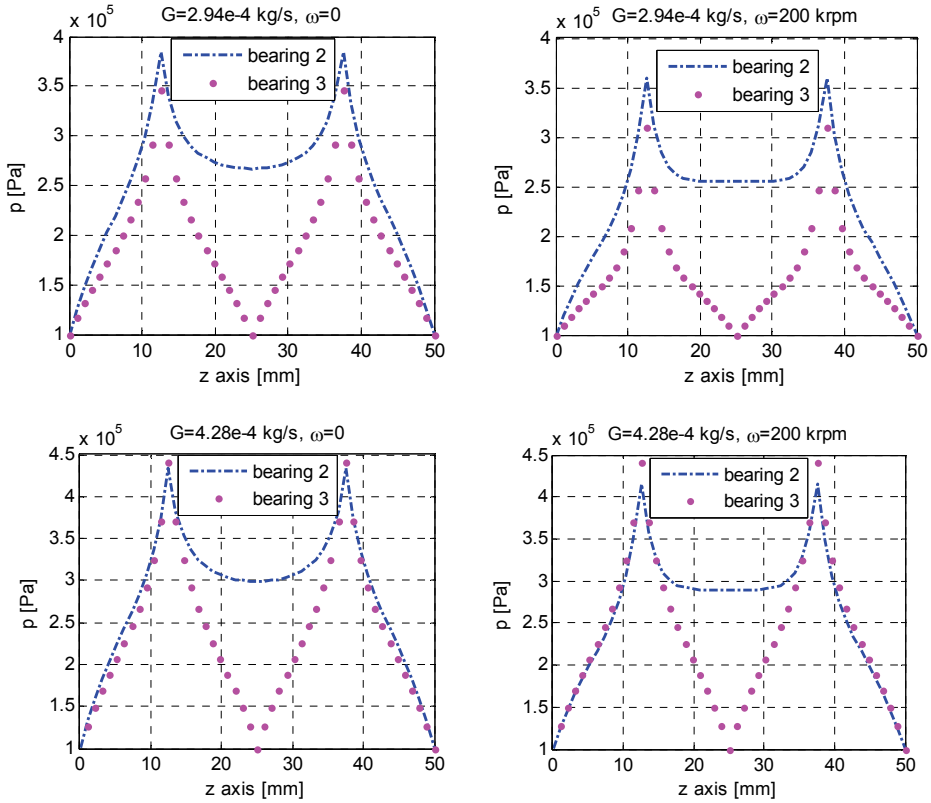

Fig. 6. Axial pressure distribution in the three bearings with ω=0 and ω=200 krpm for five different air consumption rates; restriction parameters are specified in table 2, h_0=20 μm, p_s=5·10^5 Pa rel., ε=0

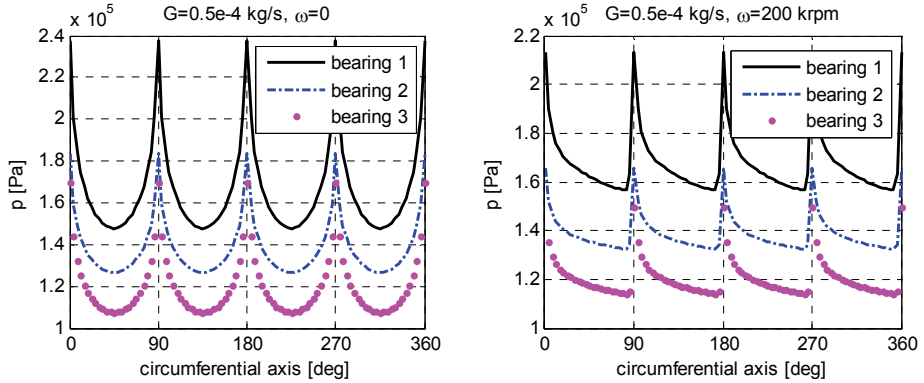

Fig. 7. Axial pressure distribution in bearing type 1 with ω=0 and ω=200 krpm for G=0.5·10^{-4} kg/s; h_0=20 μm, p_s=5·10^5 Pa rel., ε=0

is shown in figure 9 vs. Λ for the three bearings, considering different restriction parameters. Figure 9 also shows steady-state attitude angle β, calculated as follows:

$$\beta = \tan^{-1} \frac{k_{xy}}{k_{xx}} \tag{12}$$

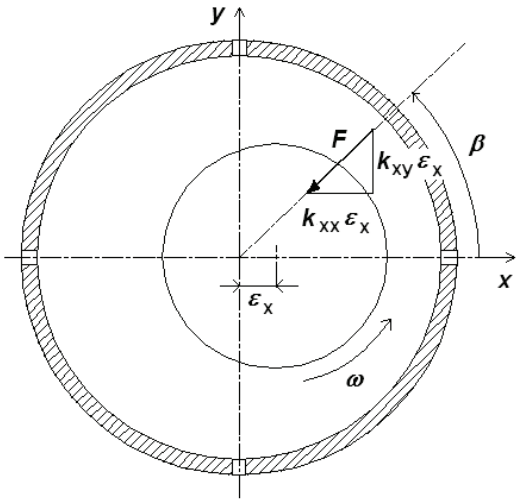

Fig. 8. Bearing reaction force on the journal in steady-state conditions due to shaft displacement along direction x

Stiffness increased with Λ up to saturation (Λ>100). At G=0.5·10-4 kg/s bearing type 1 was found to be stiffer than the other two, regardless of Λ, but at higher air consumption bearing type 2 exhibited greater stiffness at low speeds (Λ<9).

With the three bearings in sonic conditions (G=0.5·10-4 kg/s) stiffness trends do not intersect and their difference was almost constant. When bearing type 1 approached saturation ($p_c \simeq p_s$), its stiffness at low speed dropped (see case with G=1.42·10-4 kg/s). This happened also for bearing type 2, but at greater air consumptions. Stiffness at high speeds (Λ>100) always increased with G. At G=4.28·10-4 kg/s, stiffness at low speeds for bearing types 2 and 3 coincided at very low values, due to saturation of bearings.

The attitude angle, with increasing Λ, also increased from zero to a maximum and then returned to zero. The extent of maximum depended on the difference between bearing stiffness at low and high speeds: where this difference was high, also maximum β was high. Table 3 shows ratio $k^*(\Lambda>100)/k^*(\Lambda=0)$ for the three bearings to highlight this relationship.

4.5 Rotor trajectories

The whirl motion of the perfectly balanced rotor during rotation is represented in figure 10. The motion can be stable or unstable. In the former case the rotor is attracted toward the centre of the bushing after initial disturbance; in the latter case the bearing forces move the rotor away from central position.

bearing type	$k^*(\Lambda>100)/k^*(\Lambda=0)$	air flow $G\cdot10^4$ [kg/s]
1	2.62	0.5
2	2.71	
3	3.75	
1	2.54	1.42
2	1.82	
3	2.4	
1	5.8	2.14
2	2	
3	2.2	
2	2.5	2.94
3	2.26	
2	5.33	4.28
3	3.08	

Table 3. Ratio $k^*(\Lambda>100)/k^*(\Lambda=0)$ for the three bearings given different air consumptions G

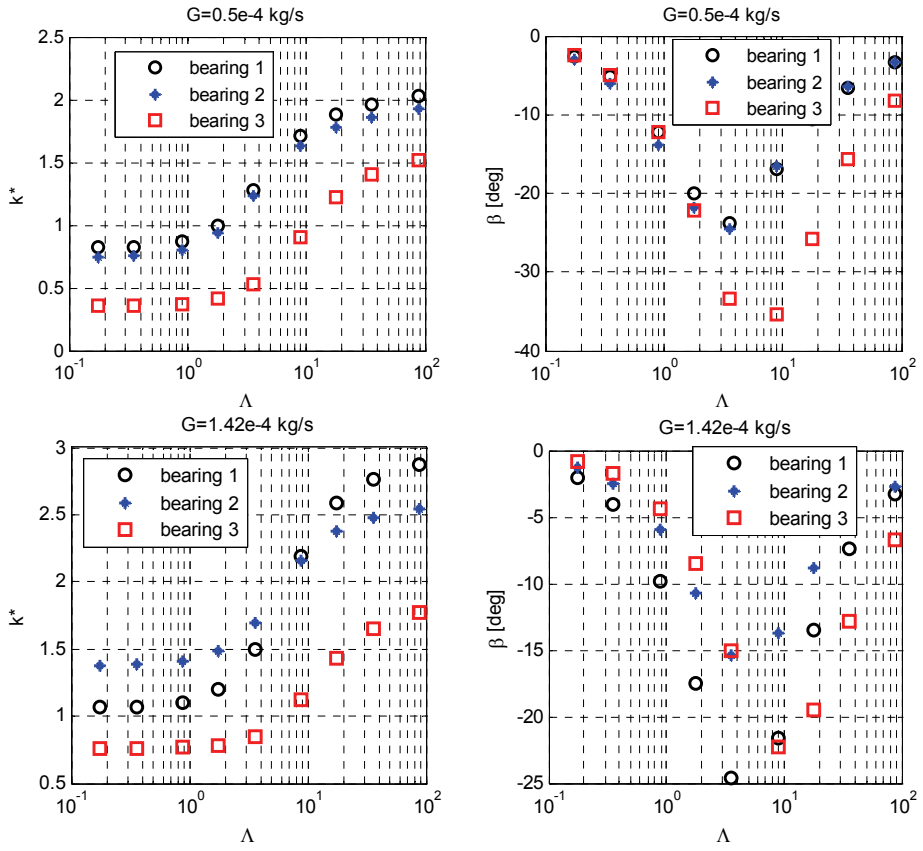

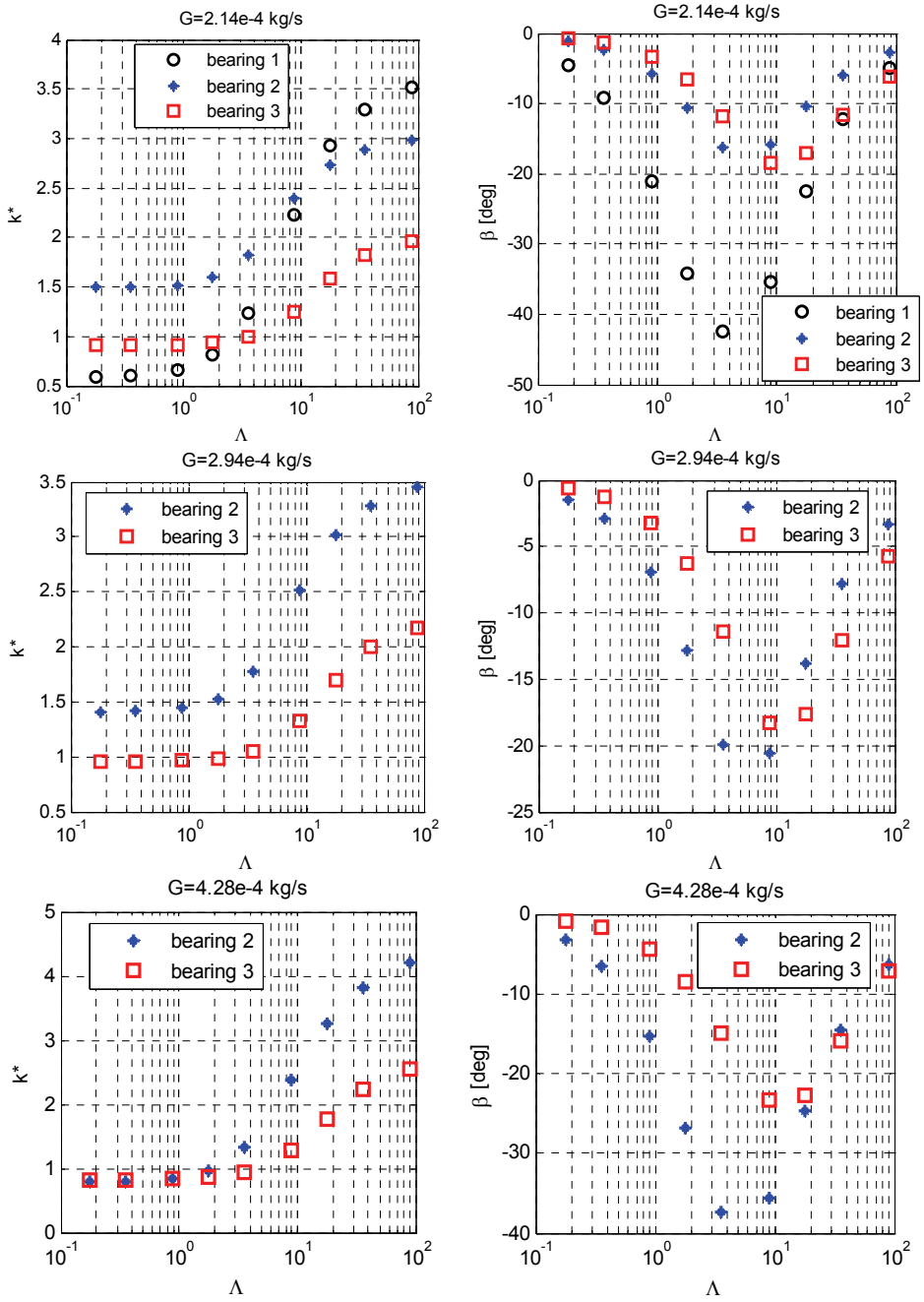

Fig. 9. Non-dimensional bearing stiffness k^* and attitude angle β vs. bearing number Λ for the three bearings

The initial condition used in the following curves are specified by

$$\varepsilon_x(0) = 0.05; \varepsilon_y(0) = 0$$

$$\dot{x}(0) = 0; \dot{y}(0) = x(0)\sqrt{\frac{k_{xx}}{m}}$$

Initial tangential speed was imposed on the rotor to produce a centrifugal force equal to the static radial force. This particular condition was adopted to decrease the simulation time required to distinguish stability from instability. In fact, with a different initial condition on $\dot{y}$, the trajectory would have been less circular, necessitating simulation of a longer transient. Stability decreased with increasing rotor mass m: figure 10 shows a comparison of rotor trajectories obtained for the same initial condition but at different values of m. The rotor-bearing system became unstable when the dynamic attitude angle turned negative, as shown in figure 11. In the stable condition the rotor angular moment, calculated relative to the centre of the bushing, decreased with time. In unstable conditions, the mechanical work done by bearing forces was found to be positive and the rotor angular moment increased (see figure 11b). The curves in figure 11 help distinguish stable versus unstable conditions, as resulting when compared to figure 10.

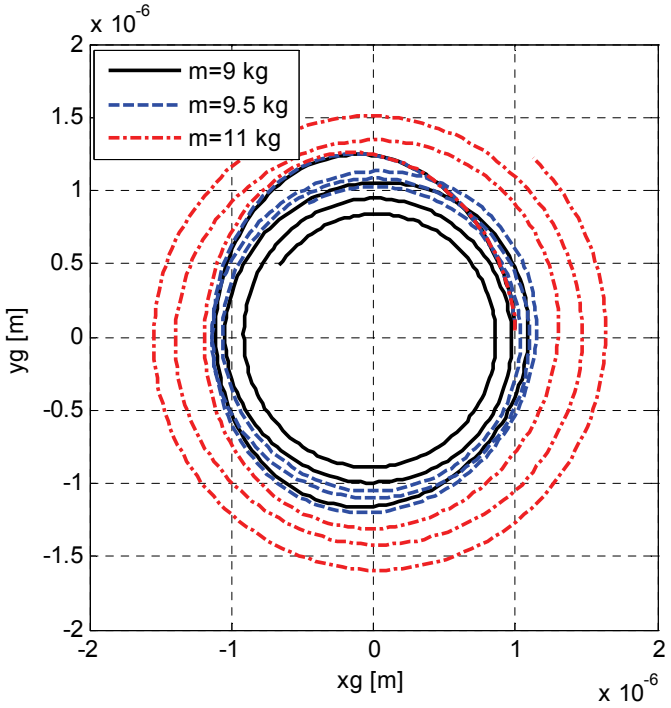

Fig. 10. Rotor trajectories with different rotor masses and initial condition $x(0)$=1 μm, $dy/dt(0)=x(0)\cdot(k_{xx}/m)^{\wedge}(0.5)$; ω=20 krpm, bearing type 1

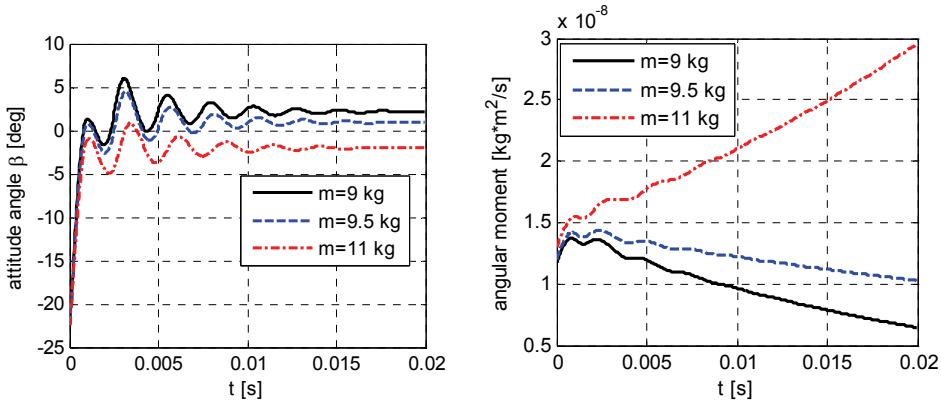

(a) (b)

Fig. 11. Attitude angle vs. time (a) and rotor angular moment vs. time (b) with different rotor masses and initial condition $x(0)$=1 μm, $dy/dt(0)=x(0)\cdot(k_{xx}/m)\text{^}(0.5)$; ω=20 krpm, bearing type 1

The three bearings are compared in figures 12 and 13, showing the rotor trajectories for identical initial condition, the attitude angle vs. time and the rotor angular moment vs. time. In this case bearing types 1 and 2 are very similar, while bearing type 3 is unstable.

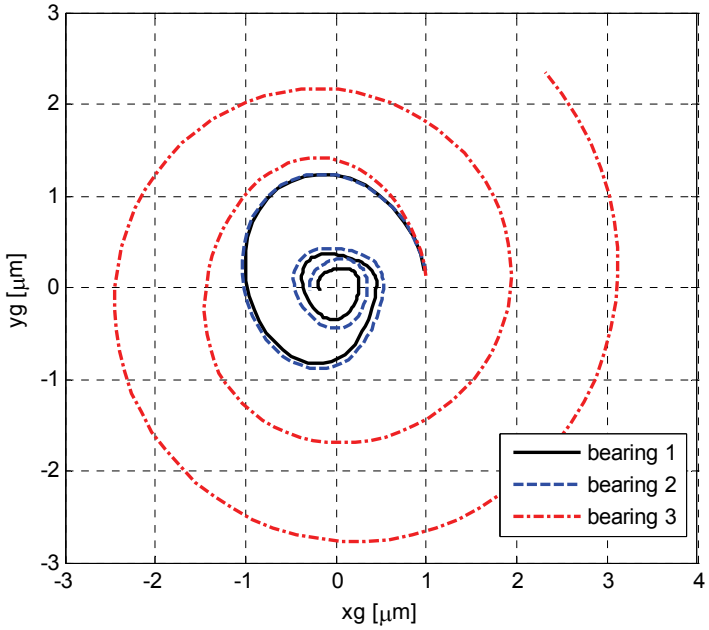

Fig. 12. Rotor trajectories with the three bearing types; m=1 kg, ω=50 krpm; initial conditions $x(0)$=1 μm and $dy/dt(0)=x(0)\cdot(k_{xx}/m)\text{^}(0.5)$.

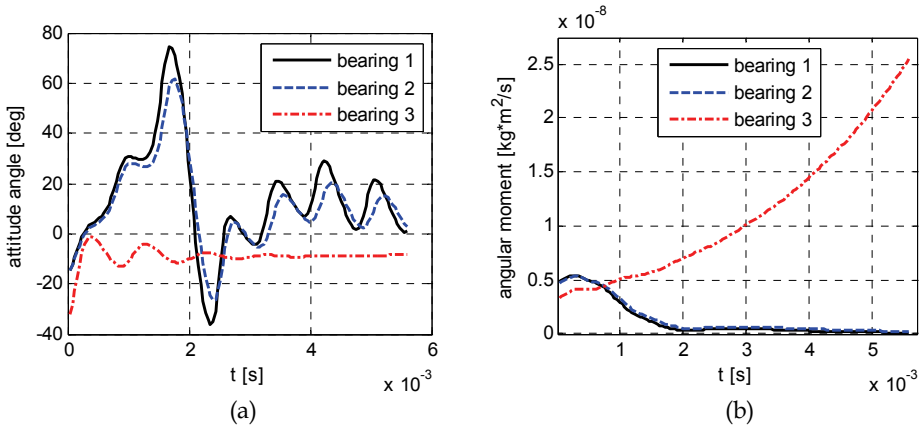

(a) (b)

Fig. 13. Attitude angle vs. time a) and rotor angular moment vs. time b) for the three bearing types; m=1 kg, ω=50 krpm; initial conditions $x(0)$=1 μm and $dy/dt(0)=x(0)\cdot(k_{xx}/m)\text{^}(0.5)$.

4.6 Bearing damping factor

Stiffness and damping coefficients of gas bearings are known to depend on bearing number Λ and also on whirl frequency ν. Stability may also be evaluated through the equivalent damping factor calculated by identifying the system with a second-order differential equation having constant coefficients:

$$m\ddot{x} + c\dot{x} + kx = 0 \tag{13}$$

The damping factor is expressed by

$$\zeta = \frac{c}{2\sqrt{km}} \tag{14}$$

and the radial coordinate of the journal centre is

$$r = r(0)e^{-\zeta\omega_n t} \tag{15}$$

where the natural frequency is

$$\omega_n = \sqrt{\frac{k}{m}} \tag{16}$$

The journal motion is stable when described by a spiral which decreases with time. In this case ζ is positive. When the damping factor is negative the spiral increases with time.
Figure 14 shows damping factor ζ vs. m for G=0.5·10-4 kg/s. In this case bearing type 3 exhibited lower damping capacity than the other bearings.

4.7 Whirl ratio

The shaft whirl frequency vs. m is shown in figure 15 for G=0.5·10-4 kg/s. The whirl frequency decreases with m and increases with ω. The rotor mass at stability threshold is

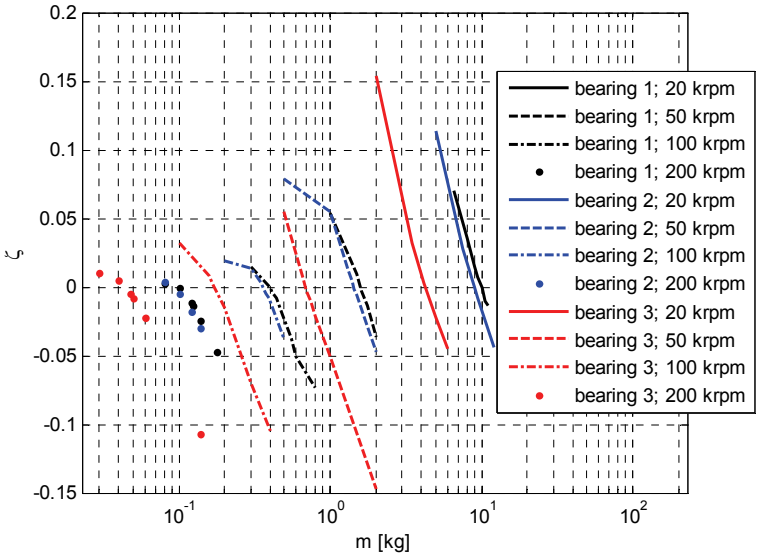

Fig. 14. Damping factor vs. rotor mass at different rotating speeds; G=0.5·10-4 kg/s

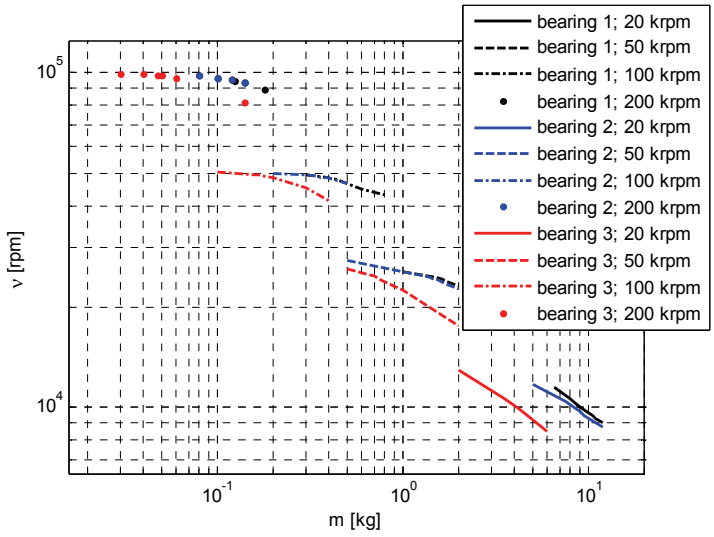

Fig. 15. Whirl frequency ν vs. m at different rotating speeds; G=0.5·10-4 kg/s

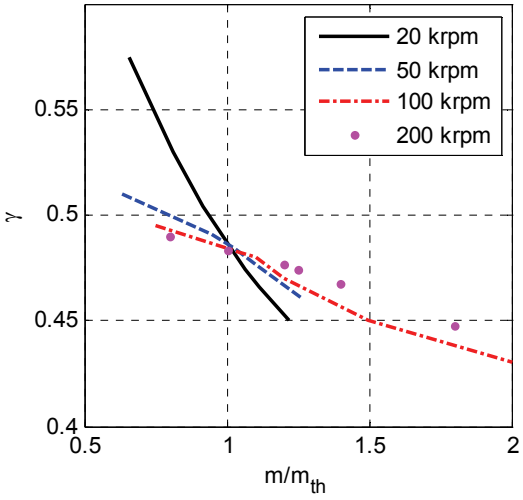

Fig. 16. Whirl ratio γ vs. m/m_{th} at different speeds; bearing type 1, G=0.5·10^{-4} kg/s

indicated as m_{th}. Figure 16 shows whirl ratio γ vs. ratio m/m_{th}. At the stability threshold it is slightly lower than 0.5 and decreases with shaft mass m.

4.8 Stability threshold

Figure 17 shows rotor mass m vs bearing number Λ at the stability threshold for the three bearings. On logarithmic axes the curves are linear and may be expressed by

$$\log_{10} m - \log_{10} m_0 = \alpha\left(\log_{10} \Lambda - \log_{10} \Lambda_0\right) \tag{17}$$

where m_0 and Λ_0 refer to a reference condition. Angular coefficient α is -2 approx. From this equation we obtain the following relation:

$$\frac{m}{m_0} = \left(\frac{\Lambda}{\Lambda_0}\right)^{\alpha} \tag{18}$$

The stability thresholds with different inherence parameters were found to be similar, but translated to different mass values.

4.9 Comparison of bearing types at different restriction parameters

Figure 18 shows the trends of bearing stiffness vs. G for ω=0 rpm and ω=200 krpm, and figure 19 shows critical journal mass m_{th} vs. G. The order of preference of the bearings changes when different air consumption rates are considered.

If stiffness at low bearing numbers is the most important parameter, bearing type 1 is the best option only for G≤0.5·10^4 kg/s, in other cases bearing type 2 is to be preferred. If it is important to maximize the bearing stiffness at high bearing numbers bearing type is to be chosen.

Considering the stability threshold, bearing type 2 is the best one for G>0.5·10^4 kg/s, while for G≤0.5·10^4 kg/s bearing 1 is to be preferred.

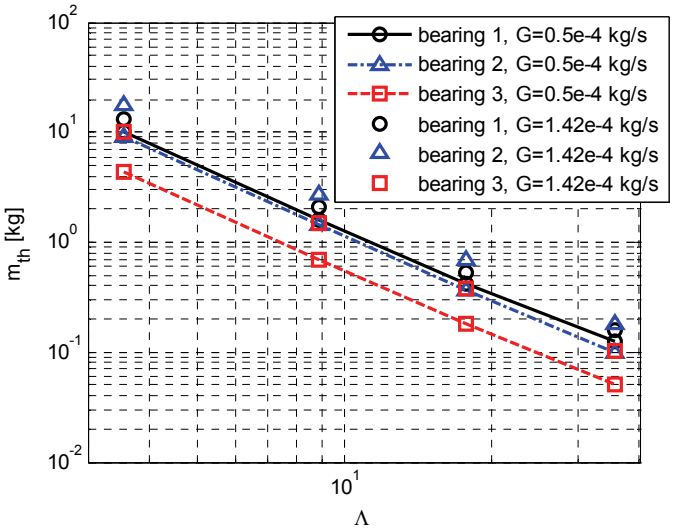

Fig. 17. Rotor mass m at stability threshold vs. bearing number Λ for the three bearings

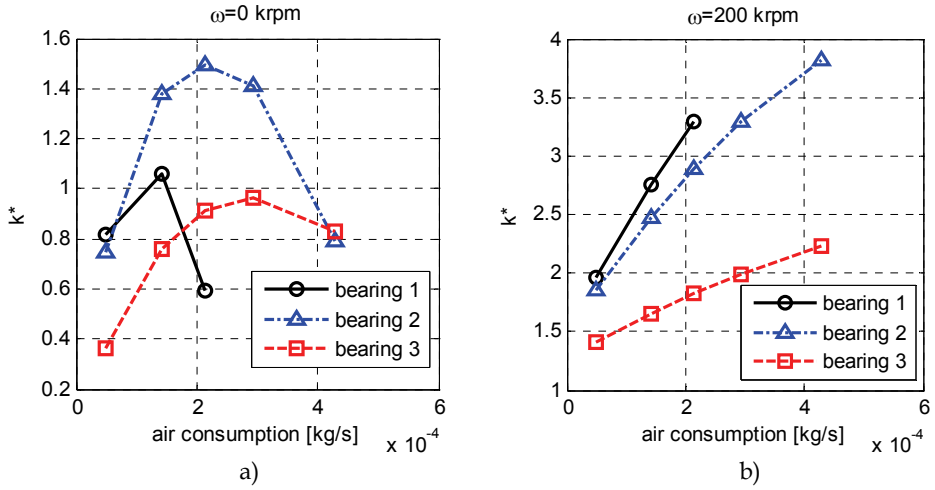

Fig. 18. Bearing stiffness k^* vs. air consumption for the three bearings; a) ω=0 rpm, b) ω=200 krpm

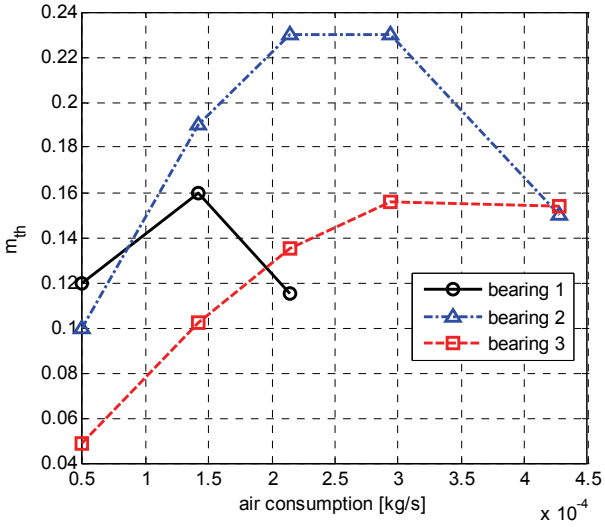

Fig. 19. Rotor mass at stability threshold vs. air consumption for the three bearings

5. Conclusion

Three bearing types were compared for different restriction parameters.
Bearing type 1 featured four supply ports situated in the bearing centre plane. Bearing type 2 featured two sets of supply ports, situated at $z=L/4$ and $z=3L/4$. Bearing type 3 also featured a central vented circumferential chamber.
The following conclusions were drawn:

- bearing type 2 in general is to be preferred to the other bearing types because of the higher stiffness and stability threshold at equal air consumption;
- with increasing Λ, the attitude angle went from zero to max. subsequently returning to zero; max. value was proportional to the difference between bearing stiffness at low and at high speeds;
- at the stability threshold the whirl ratio was slightly lower than 0.5;
- the curve of m_{th} vs. Λ on the logarithmic axes was linear and with changing restriction parameters the shaft critical mass changed by a factor regardless of speed.

6. List of symbols

D	bearing diameter
F	bearing force on journal
G	air mass flow rate
L	bearing axial length
R_s	pneumatic resistance of the supply hole
R_h	pneumatic resistance of clearance
R^0	gas constant, in calculations R^0=287.6 m^2/s^{2}K
Re	Reynolds number
T^0	absolute temperature, in calculations T^0=288 K

b ratio of critical pressure to admission pressure, b=0.528
c damping coefficient
c_d supply hole discharge coefficient
h local air clearance
h_0 clearance with rotor in centred position
k bearing radial stiffness
k^* non-dimensional bearing radial stiffness
m rotor mass
m_{th} rotor mass at stability threshold
n,m number of nodes along axial and circumferential directions
x,y,z cartesian coordinates
p_a ambient pressure
p_c supply hole downstream pressure
p_s bearing supply pressure
r,θ,z cylindrical coordinates
t time
Λ bearing number, $\Lambda=6m\omega/p_a\cdot(D/2h_0)^2$
β steady attitude angle
γ whirl ratio, $\gamma=\nu/\omega$
ε eccentricity ratio
μ dynamic viscosity, in calculations $\mu=17.89\cdot10^{-6}$ Pa·s
ν whirl frequency
ζ bearing damping factor
ω rotor angular speed

7. References

Andres, L.S. (1990). Approximate analysis of turbulent hybrid bearings, static and dynamic performance for centered operation. *ASME Journal of Tribology,* Vol. 112, 692-698.

Belforte, G.; Raparelli, T.; Viktorov, V. (1999). Theoretical investigation of fluid inertia effects and stability of self-acting gas journal bearings. *ASME Journal of Tribology*, Vol. 121, 836-843.

Belforte, G.; Raparelli, T.; Viktorov, V.; Trivella, A. (2008). Discharge coefficients of orifice-type restrictor for aerostatic bearings, *Tribology International*, Vol. 40, 512-521.

Cheng, H.S.; Pan, C.H.T. (1965). Stability analysis of gas-lubricated, self-acting, plain, cylindrical, journal bearings of finite length, using Galerkin's method. *ASME Journal of Basic Engineering*, 185-192.

Colombo, F.; Raparelli, T.; Viktorov, V. (2009). Externally pressurized gas bearings: a comparison between two supply holes configurations. *Tribology International,* Vol. 42, 303-310.

Gross, W.A.; Zachmanaglou, E.C. (1961). Perturbation solutions for Gas lubricating films. *Trans ASME, Journal of Basic Engineering*, Vol. 83, 139-144.

Han, D.C.; Park, S.S.; Kim, W.J.; KimJ.W. (1994). A study on the characteristics of externally pressurized gas bearings. *Precision Engineering*, Vol. 16, No. 3, 164-173.

Heller, S.; Shapiro, W.; Decker, O. (1971). A porous hydrostatic gas bearing for use in miniature turbomachinery. *ASLE Transactions*, 144-155.

Lund, J.W. (1968). Calculation of stiffness and damping properties of gas bearings. *ASME Journal of Lubrication Technology,* 793-803.

Sawicki, J.T.; Capaldi, R.J.; Adams, M.L. (1997). Experimental and theoretical rotordynamic characteristics of a hybrid journal bearing. *ASME Journal of Tribology,* Vol. 119, 132-141.

Su, J.C.T.; Lie, K.N. (2003). Rotation effects on hybrid air journal bearings. *Tribology International,* Vol. 36, 717-726.

Su, J.C.T.; Lie, K.N. (2006). Rotor dynamic instability analysis on hybrid air journal bearings. *Tribology International*, Vol. 39, No. 1, 238-248.

Sun, D.C. (1975). Stability of gas-lubricated, externally pressurized porous journal bearings. *ASME Journal of Lubrication Technology*, 494-505.

Wadhwa, S.S.; Sinhasant, R.; Singh, D.V. (1983). Analysis of orifice compensated externally pressurized gas bearing. *Tribology International,* Vol. 16, No. 4, 203-211.

Yang, D.W.; Chen, C.H.; Kang Y.; Hwang, R.M.; Shyr, S.S. (2009). Influence of orifices on stability of rotor-aerostatic bearing system. *Tribology International,* Vol. 42, 1206-1219.

Yoshikawa, H.; Ota, T.; Higashino, K.; Nakai, S. (1999). Numerical analysis on dynamic characteristics of cryogenic hydrostatic journal bearing. *ASME Journal of Tribology,* Vol. 121, 879-885.

Zhang, R.Q.; Chang, H.S. (1995). A new type of hydrostatic/hydrodynamic gas journal bearing and its optimization for maximum stability. *Tribology Transactions,* Vol. 38, No. 3, 589-594.

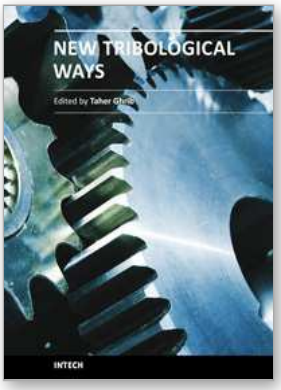

New Tribological Ways

Edited by Dr. Taher Ghrib

ISBN 978-953-307-206-7
Hard cover, 498 pages
Publisher InTech
Published online 26, April, 2011
Published in print edition April, 2011

This book aims to recapitulate old information's available and brings new information's that are with the fashion research on an atomic and nanometric scale in various fields by introducing several mathematical models to measure some parameters characterizing metals like the hydrodynamic elasticity coefficient, hardness, lubricant viscosity, viscosity coefficient, tensile strength .... It uses new measurement techniques very developed and nondestructive. Its principal distinctions of the other books, that it brings practical manners to model and to optimize the cutting process using various parameters and different techniques, namely, using water of high-velocity stream, tool with different form and radius, the cutting temperature effect, that can be measured with sufficient accuracy not only at a research lab and also with a theoretical forecast. This book aspire to minimize and eliminate the losses resulting from surfaces friction and wear which leads to a greater machining efficiency and to a better execution, fewer breakdowns and a significant saving. A great part is devoted to lubrication, of which the goal is to find the famous techniques using solid and liquid lubricant films applied for giving super low friction coefficients and improving the lubricant properties on surfaces.

INTECH
open science | open minds

InTech Europe
University Campus STeP Ri
Slavka Krautzeka 83/A
51000 Rijeka, Croatia
Phone: +385 (51) 770 447
Fax: +385 (51) 686 166
www.intechopen.com

InTech China
Unit 405, Office Block, Hotel Equatorial Shanghai
No.65, Yan An Road (West), Shanghai, 200040, China
中国上海市延安西路65号上海国际贵都大饭店办公楼405单元
Phone: +86-21-62489820
Fax: +86-21-62489821